Nanoscale Research Letters
a SpringerOpen Journal

NANO EXPRESS Open Access

Consistent melting behavior induced by Joule heating between Ag microwire and nanowire meshes

Kaoru Tsuchiya, Yuan Li* and Masumi Saka

Abstract

The melting behavior of an Ag microwire mesh induced by Joule heating was numerically investigated and compared with that of the corresponding Ag nanowire mesh with the same structure but different geometrical and physical properties of the wire itself. According to the relationship of melting current and melting voltage during the melting process, a similar repetitive zigzag pattern in melting behavior was discovered in both meshes. On this basis, a dimensionless parameter defined as figure of merit was proposed to characterize the current-carrying ability of the mesh. The consistent feature of figure of merit in both meshes indicates that the melting behavior of the Ag nanowire mesh can be predicted from the present results of the corresponding Ag microwire mesh with the same structure but made from a different wire (e.g., different size, different material) through simple conversion. The present findings can provide fundamental insight into the reliability analysis on the metallic nanowire mesh-based transparent conductive electrode.

Keywords: Consistent feature; Figure of merit; Joule heating; Melting behavior; Ag microwire/nanowire mesh; Transparent conductive electrode

Background

To meet the requirement of next-generation flexible optoelectronics for both information (e.g., display, electronic reader, touch screen) and energy (e.g., solar cell, window glass), there is growing interest to develop transparent conductive electrodes (TCEs) possessing high optical transmission, good electrical conductivity, and excellent flexibility [1,2]. However, the present common commercial TCE material, i.e., indium tin oxide (ITO), suffers from several major limitations [3-5], such as high cost due to the shortage of indium and poor mechanical stability due to the brittleness. Therefore, it is highly desirable to find a promising alternative which can be used in the forthcoming TCEs [6]. Recently, the network of various nanostructured materials (e.g., carbon nanotube [7,8], graphene [9-11], metallic nanowire [12-20] /nanotrough [21] /honeycomb [22], and the combinations of the above [3,23-25]) has shown great potential for the application in optoelectronic devices such as solar cells [9,16-18] and touch screens [14,20].

Here, our focus is on metallic nanowire mesh (i.e., regular nanowire network) because of its ideal characteristics of low sheet resistance, high optical transparency, and flexible controllability. For example, Kang et al. [16] have fabricated a Cu nanowire mesh electrode on a polyethylene terephthalate (PET) substrate, which shows compatible optical transmittance in the visible wavelength range with commercial ITO-coated PET and offers lower sheet resistance than ITO. Moreover, the short-circuit current and power conversion efficiency of a solar cell with this type of Cu nanowire mesh electrode are comparable to those of the same device using an ITO electrode.

However, realizing the potential benefits of such metallic nanowire mesh in practical optoelectronic devices remains a great challenge because of the lack of reliability analysis. It is known that the pathway of current in a metallic nanowire mesh remains in the nanowire itself, instead of uniform distribution throughout the whole ITO film. Great reduction in current flow area will cause

* Correspondence: liyuan@ism.mech.tohoku.ac.jp
Department of Nanomechanics, Tohoku University, Aoba 6-6-01, Aramaki, Aoba-ku, Sendai 980-8579, Japan

enormous increase in current density and significant rise in temperature due to Joule heating. Therefore, it is believed that the melting induced by Joule heating is a potential threat to the degradation of the metallic nanowire mesh-based TCE, which may cause deterioration of the corresponding optoelectronic devices. In a pioneering experimental report, Khaligh and Goldthorpe [26] have indicated that at a constant current density, a random Ag nanowire network fails after a certain period. Moreover, the network with higher sheet resistance carrying greater current density will fail more easily because of Joule heating. Hereafter, a numerical method has been developed [27] by the present authors to clarify the melting behavior of metallic nanowire mesh due to Joule heating. Using this technique, a repetitive zigzag pattern in the relationship of melting current and melting voltage triggering the melting of the mesh was discovered. It indicates that in real working conditions, a metallic nanowire mesh supplied with current source may experience repetitive unstable (where several wires are melted simultaneously at a constant current/voltage) and stable (where an increment of current/voltage is necessary for melting progression) melting behavior until the mesh is open. However, some of these predicted intrinsic features in the melting of the metallic nanowire mesh would not be detectable because of the difficulty in sample preparation and experimental measurement.

To overcome the above weakness, the relatively easy-to-prepare microwire mesh comes into the sight. One might expect the melting behavior of microwire and nanowire meshes to be similar by assuming that the currents would just scale up. However, metallic nanowire in general displays different properties from microwire because of significant size effect. For example, with decreasing dimension, melting point and thermal conductivity decrease while electrical resistivity increases. Such differences make it difficult to insist on the similarity of the melting behavior for microwire and nanowire meshes, even if both of which have the same structure under the same working conditions.

Herein, to find the intrinsic relationship of the melting behavior between metallic microwire and nanowire meshes, the melting behavior of an Ag microwire mesh was numerically investigated and compared to that of the corresponding Ag nanowire mesh, which has the same mesh structure but different geometrical and physical properties of the wire itself. A similar zigzag pattern was observed in the relationship between melting current and melting voltage of both meshes. Therefore, a dimensionless parameter defined as figure of merit was proposed to indicate the current-carrying ability of the mesh. The consistent figure of merit during the whole melting process of both meshes implies that the melting behavior of the nanowire mesh is predictable from that of the microwire mesh by simple conversion. The present findings provide fundamental insight into the reliability analysis on the metallic nanowire mesh hindered by difficult sample preparation and experimental measurement, which will be helpful to develop ideal metallic nanowire mesh-based TCE with considerable reliability.

Methods

A previous numerical method [27] was employed to investigate the melting behavior of an Ag microwire mesh and compared with that of the corresponding nanowire mesh which has the same mesh structure (e.g., pitch size, segment number, and boundary conditions) but different geometrical and physical properties of the wire itself (e.g., cross-sectional area, thermal conductivity, electrical resistivity, and melting point).

The mesh structure is illustrated in Figure 1. It is a regular network with 10 columns and 10 rows, which indicates that the mesh size M@N is 10@10. The pitch size l is 200 μm, making the mesh area S of 3.24×10^6 μm^2. A mesh node (i, j) denoted by integral coordinates $(0 \le i \le M-1,\ 0 \le j \le N-1)$ is the intersection of the $(i+1)$th column and the $(j+1)$th row in the mesh. A mesh segment is the wire between two adjacent mesh nodes. For simplicity, the segments on the left, right, downside, and upside of the mesh node (i, j) are denoted by $S^{L}_{(i,j)}$, $S^{R}_{(i,j)}$, $S^{D}_{(i,j)}$, and $S^{U}_{(i,j)}$, respectively. Obviously, there are $M \times N = 100$ mesh nodes and $M(N-1) + N(M-1) = 180$ mesh segments.

The electrical boundary conditions are also shown in Figure 1. The load current I is input from node (0, 0) and is output from node (9, 0) with zero electrical potential at node (9, 9). Moreover, there is no external input/output current for all the other nodes. For the thermal boundary conditions, the temperature of the peripheral nodes (i.e., $(i, 0)$, $(0, j)$, $(i, 9)$, $(9, j)$) is set at room temperature (RT, $T_0 = 300$ K), while there is no external input/output heat energy for all the other nodes.

The geometrical and physical properties of the wires are listed in Table 1. Here, A is the cross-sectional area

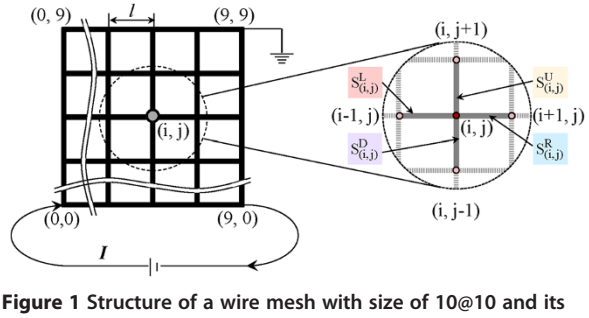

Figure 1 Structure of a wire mesh with size of 10@10 and its electrical boundary conditions.

Table 1 Geometrical and physical properties of the wires

	Ag microwire	Ag nanowire	Al nanowire
Side length, w (μm)	1.000	0.1000	0.1000
Cross-sectional area, A ($\times 10^{-2}$ μm^2)	100.0	1.000	1.000
Melting point, T_m ($\times 10^3$ K)	1.234	0.873 [30] (exp.)	0.736 [31] (num.)
Thermal conductivity at RT, λ ($\times 10^{-4}$ W/μm·K)	4.200	3.346 [28] (num.)	1.150 [32] (num.)
Electrical resistivity at RT, ρ_0 ($\times 10^{-2}$ Ω·μm)	1.590	11.90 [29] (exp.)	6.20 [32] (exp.)
Electrical resistivity at T_m, ρ_m ($\times 10^{-2}$ Ω·μm)	7.200	37.80	17.72

calculated from the side length w of the wire with the square cross section, T_m is the melting point, λ is the thermal conductivity, and ρ is the electrical resistivity with the subscripts '0' and 'm' representing the value at T_0 and T_m. Note that ρ_m [$=\rho_0\{1 + \alpha(T_m - T_0)\}$] is calculated by using the temperature coefficient of resistivity α. Note that the bulk values of Ag were employed for the microwire, while size effect was taken into account for the nanowire. Because of electron scattering from surface and grain boundaries [28,29], the thinner the wire is, the lower T_m, λ, and electrical conductivity ($=1/\rho$) are.

To clarify the melting behavior of the mesh, the fundamental theoretical analyses [27] on the corresponding electrothermal problem is summarized in the following. First, as shown in Figure 2a, a horizontal mesh segment (i.e., a wire) $S^L_{(i,j)}$ between node $(i - 1, j)$ and (i, j) with an electrically and thermally insulated surface was considered, where the current flows from node $(i - 1, j)$ to (i, j). Based on Ohm's law, the current density j in the mesh segment can be calculated as

$$j = -\frac{1}{\rho}\frac{d\phi}{dx}. \tag{1}$$

Here, ϕ is the electrical potential, and x is the axial coordinate in the mesh segment with the direction rightward for horizontal segment and upward for vertical segment. Using Fourier's law, the heat flux q in $S^L_{(i,j)}$ can be calculated as

$$q = -\lambda\frac{dT}{dx}, \tag{2}$$

where T is temperature.

By ignoring heat transfer of the mesh to the underlying substrate for simplicity, the heat conduction equation can be given as

$$\lambda\frac{d^2T}{dx^2} + \rho j^2 = 0. \tag{3}$$

Assuming that the temperatures of nodes $(i - 1, j)$ and (i, j) are $T_{(i-1,j)}$ $(x = 0)$ and $T_{(i,j)}$ $(x = l)$, temperature distribution in the mesh segment $S^L_{(i,j)}$ can be obtained by solving Equation 3 as

$$T = -\frac{\rho}{2\lambda}j^2x^2 + \left\{\frac{T_{(i,j)} - T_{(i-1,j)}}{l} + \frac{\rho l}{2\lambda}j^2\right\}x + T_{(i-1,j)}. \tag{4}$$

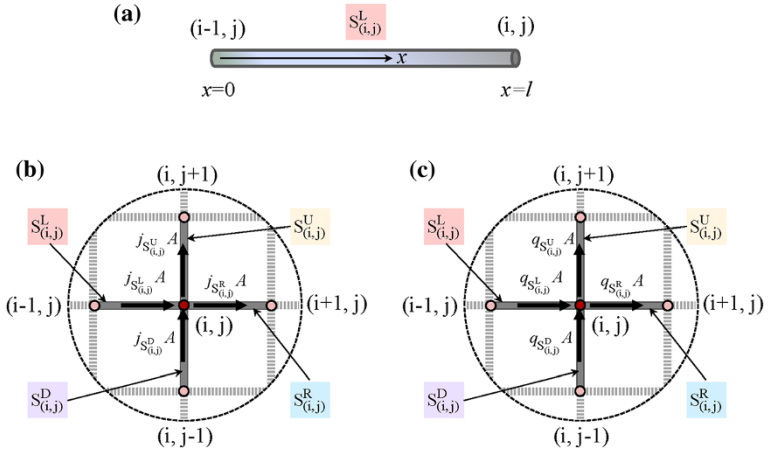

Figure 2 Theoretical analysis on the electrothermal problem of the wire mesh. (a) Mesh segment, **(b)** current passing through mesh node (i, j), and **(c)** heat energy passing through mesh node (i, j).

Note that in the present simulation, ρ_m was used for ρ to approximate real condition neglecting the effect of the temperature dependence of electrical resistivity.

Second, as shown in Figure 2b,c, the current and heat energy passing through a mesh node (i, j) with four adjacent nodes were considered. In Figure 2b, the current is assumed to flow rightward in the horizontal direction and upward in the vertical direction. According to Kirchhoff's current law, we have

$$I_{\text{external}} + I_{\text{internal}} = 0. \tag{5}$$

Here, I_{external} is the external input/output current at node (i, j), and I_{internal} is the sum of internal currents flowing through the node (i, j) from its four adjacent nodes. By assuming that the current flowing into the node is positive and the current flowing out of the node is negative, we can obtain

$$I_{\text{internal}} = \left\{ j_{S^{\text{L}}_{(i,j)}} - j_{S^{\text{R}}_{(i,j)}} + j_{S^{\text{D}}_{(i,j)}} - j_{S^{\text{U}}_{(i,j)}} \right\} A, \tag{6}$$

where the subscript of j denotes the corresponding mesh segment. Taking into account a system of linear equations for the node (i, j) composed of Equations 1, 5, and 6, the current density in any mesh segment can be obtained. Similarly, according to the law of the conservation of heat energy, we have

$$Q_{\text{external}} + Q_{\text{internal}} = 0. \tag{7}$$

Here, Q_{external} is the external input/output heat energy at node (i, j), and Q_{internal} is the sum of the internal heat energy transferred to node (i, j) from its four adjacent nodes. In Figure 2c, by assuming that the incoming heat energy is positive and the outgoing heat energy is negative, we have

$$Q_{\text{internal}} = \left\{ q_{S^{\text{L}}_{(i,j)}} - q_{S^{\text{R}}_{(i,j)}} + q_{S^{\text{D}}_{(i,j)}} - q_{S^{\text{U}}_{(i,j)}} \right\} A. \tag{8}$$

Taking into account a system of linear equations for the node (i, j) composed of Equations 2, 7, and 8, the temperature at any mesh node can be obtained. Finally, by substituting the above obtained current density in any mesh segment and temperature at any mesh node into Equation 4, the temperature distribution in any mesh segment can be monitored.

A synopsis of the corresponding computational algorithm [27] is provided as below. Initially, a small value is assigned to the input current I. The corresponding maximum temperature in the mesh $T_{\max}$ can be identified, which rises with the increasing I. By gradually increasing I with increment ΔI to make $T_{\max}$ reach T_m, the first mesh segment melts and breaks from an arbitrary small force occurring in actual operation (e.g., vibration). At that time, the input current and the voltage between node (0, 0) and node (9, 0) are recorded as melting current I_m and melting voltage V_m. The corresponding resistance R_m of the mesh can be calculated by dividing V_m by I_m. It should be noted that ΔI must be small enough so that melting segment can melt one by one as far as possible. Subsequently, an ultra-small value is assigned to the cross-sectional area of the first melted mesh segment in order to approximate zero. The pathway of the current and heat in the mesh is therefore renewed. By repeating the aforementioned process, the current triggering the melting of mesh segment one by one can be obtained until the mesh becomes open. Therefore, the relationship between I_m and V_m as well as the variation of R_m with the number n_b of the broken mesh segments can be obtained over the entire melting process of the mesh.

Results and discussion

Melting behavior of the Ag microwire mesh

As shown in Figure 3a,b, the obtained relationship of melting current I_m and melting voltage V_m as well as the variation of mesh resistance R_m with the number n_b of

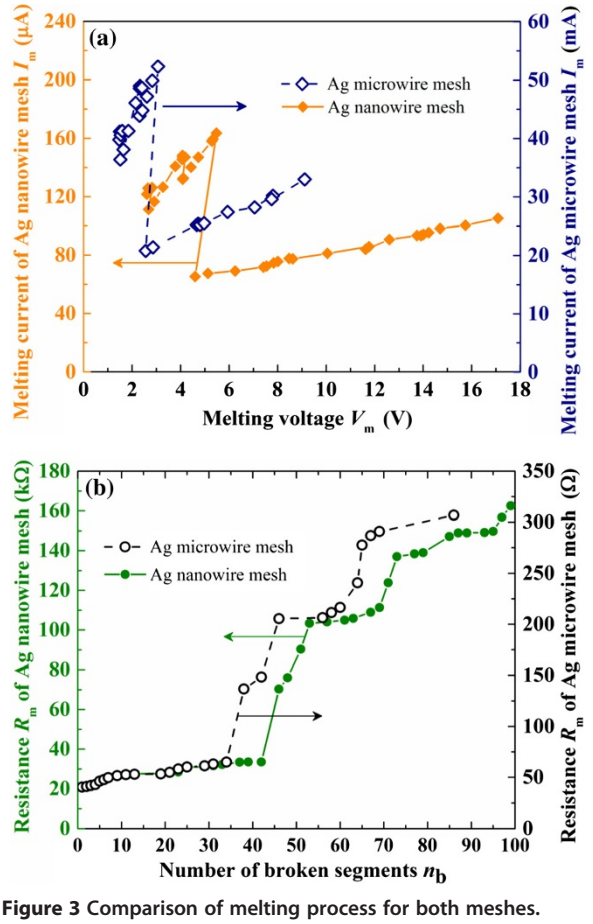

Figure 3 Comparison of melting process for both meshes. **(a)** The relationship between I_m and V_m, and **(b)** the variation of R_m with n_b.

broken mesh segments during the entire melting process of the Ag microwire mesh is compared with those of the corresponding Ag nanowire mesh, respectively.

Obviously, a repetitive zigzag pattern is observed in the relationship of I_m and V_m in the Ag microwire mesh, which demonstrates the repetition of three different trends: increase of both I_m and V_m, decrease of both I_m and V_m, and decrease of I_m but increase of V_m. Such pattern in the melting behavior of Ag microwire mesh is similar with that of the corresponding Ag nanowire mesh [27]. Note that the microwire mesh has higher I_m but lower V_m than the nanowire mesh, because the microwire has larger cross-sectional area and lower resistivity (see Table 1) and therefore lower electrical resistance (see Figure 3b) than the nanowire.

During the melting process, the symmetrical mesh structures at three special moments for both meshes are compared in Figure 4. The difference in the melting

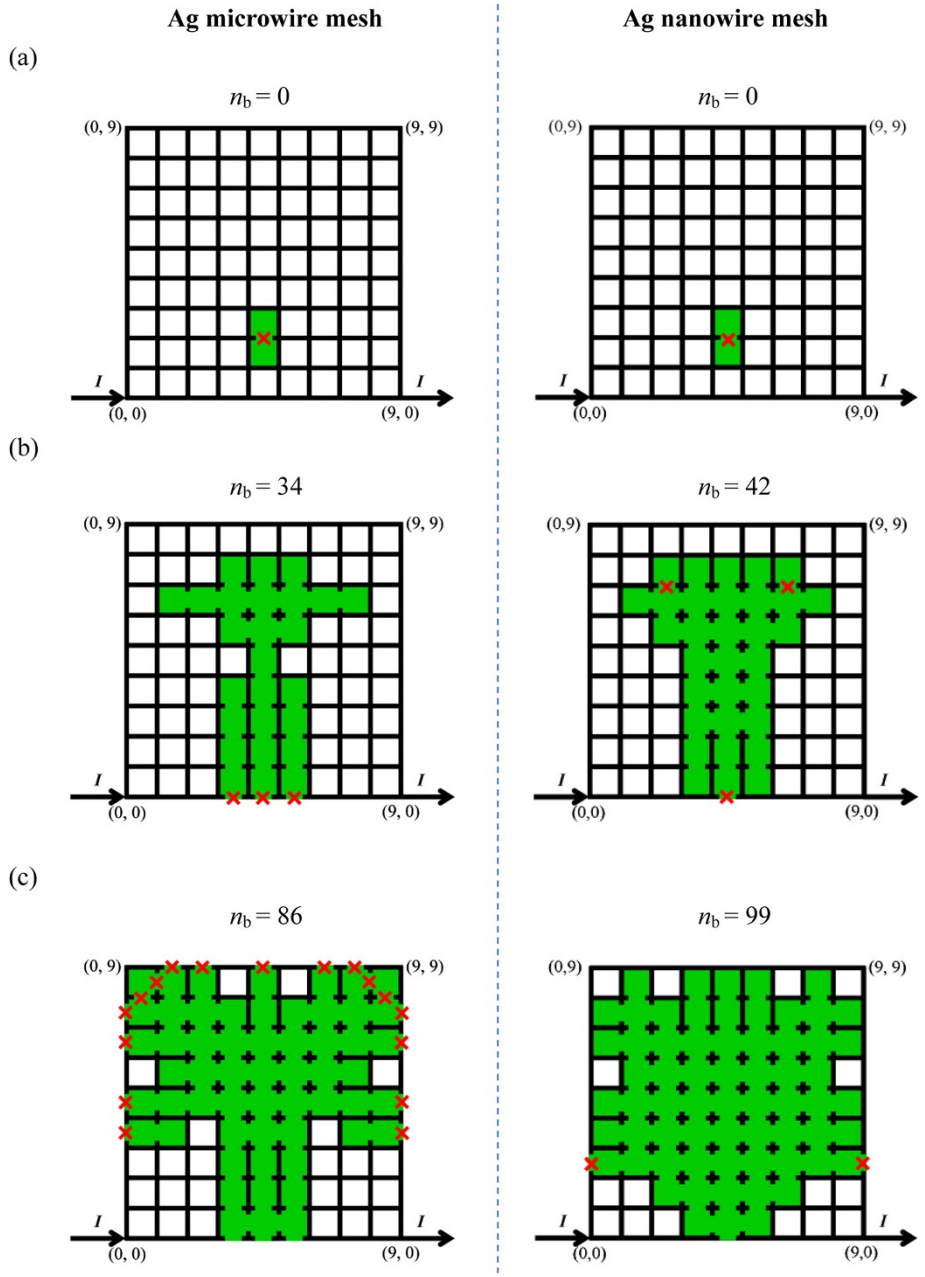

Figure 4 Mesh structures at three special moments in the melting process of both meshes. (a) The starting moment, **(b)** the moment with the maximum current (i.e., sudden fall of current), and **(c)** the ending moment.

pathway of both meshes can be attributed to the different ΔI for monitoring the melting of mesh segment, which are 0.1 mA for the Ag microwire mesh and 0.1 μA for the Ag nanowire mesh. Note that such difference can be removed by employing much smaller ΔI for the Ag microwire mesh at the expense of increasing computational cost.

Moreover, from the present simulation results, it is believed that under constant current density (i.e., current-controlled current source), electric breakdown of the mesh will never happen as long as the load current I does not reach the maximum value of I_m (i.e., I_{mC}) even if several mesh segments melt. This point is quite different from the reported electrical failure of a random Ag nanowire network [26] under constant current density after a certain current stressing period. Such difference between experiments and present simulations also implies that the electrical failure in real Ag nanowire mesh should be the synergy of Joule heating and some other possible causes, such as corrosion by sulfur, atomic diffusion in the nanowire itself, and Rayleigh instability [26].

Proposal of figure of merit *Z*

To explore the intrinsic characteristics of the melting behavior of metallic microwire and nanowire meshes, it would be helpful to find a common parameter which is independent of geometrical and physical properties of the mesh. In order to deduce such a parameter, let us consider a simple model of a wire subjected to a constant current as shown in Figure 2a. By neglecting the difference between $T_{(i,j)}$ and $T_{(i-1,j)}$ for simple approximation, the following equation can be easily obtained from Equation 4:

$$T_C - T_{(i,j)} = j^2 \frac{\rho}{8\lambda} l^2, \tag{9}$$

where T_C is the maximum temperature occurring in the center of the wire with $x = l/2$. It indicates that $j^2 l^2 (\rho/\lambda)/(T_C - T_{(i,j)})$ is independent of geometrical and physical properties of the wire.

Based on the above consideration, the following dimensionless parameter Z was proposed as figure of merit of the mesh:

$$Z = \left(\frac{I_m}{A}\right)^2 \frac{\rho}{\lambda} \frac{S}{T_m - T_0}, \tag{10}$$

which indicates the current-carrying ability of the mesh. The variation of calculated Z during the melting process is shown in Figure 5, which was developed from the numerical results in Figure 3. Note that the maximum value of Z (i.e., Z_C) corresponding to the maximum value of I_m (i.e., I_{mC}) characterizes the current-carrying capacity of the mesh, at which the mesh equipped with current-controlled current source will melt until open. Reasonably consistent behavior of Z in both meshes can be clearly observed in Figure 5. The minor difference can be attributed to the different melting pathways (see Figure 4), which can be removed by employing much smaller ΔI for the microwire mesh with sacrifice of computational cost.

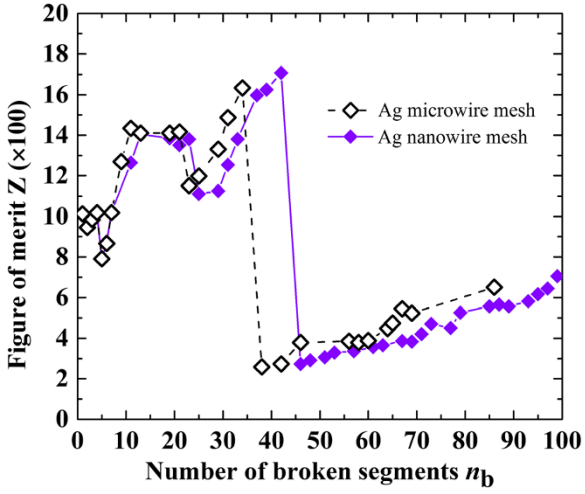

Figure 5 Variation of Z with n_b in the melting process of both meshes.

Generally, for the same material, T_m, ρ, λ, and A are dependent on wire size, while S is dependent on mesh structure. For a given mesh structure with a known S, the smaller A results in smaller T_m and λ but larger ρ, and therefore smaller I_m according to Equation 10. This point is the same with the above numerical results where the I_m of the microwire mesh is significantly higher than that of the nanowire mesh (see Figure 3a).

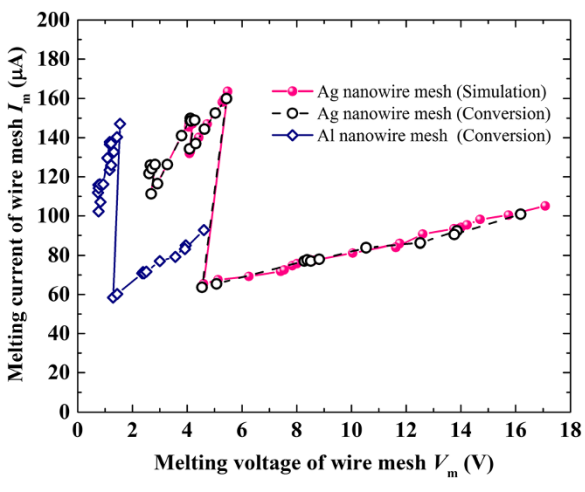

Figure 6 Predicted melting behavior of Ag and Al nanowire meshes by conversion.

Therefore, it is expected that the obtained melting behavior of the microwire mesh can be used to predict that of the wire mesh with same structure at the same working condition even if made from a different wire (i.e., different size, different material) through simple conversion with the known Z. Taking the Ag nanowire mesh as an example, the conversion process is summarized here. First, the melting current I_m for the nanowire mesh can be calculated from Equation 10 with the known Z. Second, the variation of the R_m for nanowire mesh can be calculated from that for the microwire mesh in Figure 3b as

$$R_m\Big|_{NW} = R_m\Big|_{MW} \times \left(\frac{\rho_m}{A}\right)\Big|_{NW} \times \left(\frac{A}{\rho_m}\right)|_{MW}, \qquad (11)$$

because of the same melting process. Note that '$|_{NW}$' and '$|_{MW}$' indicate the case for the Ag nanowire mesh and Ag microwire mesh, respectively. Third, the variation of V_m for the Ag nanowire mesh can be calculated by multiplying the obtained R_m and I_m from the above two steps. The predicted melting behavior of the Ag nanowire mesh derived from the above indirect conversion is shown in Figure 6, which indicates good agreement with that obtained from direct numerical simulation, and therefore validates the feasibility of the present conversion method. Figure 6 also gives the predicted melting behavior of the Al nanowire mesh with the same structure through indirect conversion. Obviously, the melting behavior of the mesh is largely dependent on the physical properties of the wire itself.

It should be noted that the present boundary conditions and mesh structure are only one example. Certainly, boundary conditions and mesh structure will have great effect on the melting behavior of the wire mesh as well as physical properties of the wire itself. However, the consistent feature in the melting behavior among the wire meshes with the same structure under the same boundary conditions will not change. Therefore, the present findings can provide meaningful insight for the experimental investigation on the reliability of the metallic nanowire mesh-based TCE.

Conclusions

In this work, the melting behavior of an Ag microwire mesh induced by Joule heating was numerically investigated and compared with that of the corresponding Ag nanowire mesh with the same mesh structure but different geometrical and physical properties of the wire itself. The repetitive zigzag pattern in the relationship of melting current and melting voltage during the melting process in the Ag microwire mesh was found to be similar with that of the Ag nanowire mesh. A dimensionless parameter Z was proposed as figure of merit to characterize the current-carrying ability of the mesh. The consistent behavior of figure of merit in both meshes indicates that the known Z and the melting behavior of the Ag microwire mesh can be used to predict the melting behavior of the nanowire mesh even with different materials (e.g., Ag nanowire mesh, Al nanowire mesh), which is hindered by the cost of sample preparation and the difficult control of ultra-low current stressing in experiments. The present findings indicate great insight for reliability analysis on the metallic nanowire mesh-based TCE, which will be beneficial to improve the performance of the corresponding optoelectronic devices.

Abbreviations

ITO: indium tin oxide; PET: polyethylene terephthalate; RT: room temperature; TCE: transparent conductive electrode.

Competing interests

The authors declare that they have no competing interests.

Authors' contributions

KT carried out the numerical analysis and drafted the manuscript. YL and MS conceived the study, participated in its design, and helped to finalize the manuscript. All authors read and approved the final manuscript.

Acknowledgements

The authors would like to thank Prof. H. Tohmyoh for his valuable discussion. This work was supported by JKA through its promotion funds from AUTORACE (25-152) and by Tohoku Leading Women's Jump Up Project for 2013 (J130000264) from the Ministry of Education, Culture, Sports, Science, and Technology (MEXT) of Japan.

Received: 10 April 2014 Accepted: 3 May 2014
Published: 15 May 2014

References

1. Ginley DS, Hosono H, Paine DC: *Handbook of Transparent Conductors*. New York: Springer; 2010.
2. Ellmer K: **Past achievements and future challenges in the development of optically transparent electrodes.** *Nat Photonics* 2012, **6:**808–816.
3. Kylberg W, de Castro FA, Chabrecek P, Sonderegger U, Chu BTT, Nuesch F, Hany R: **Past achievements and future challenges in the development of optically transparent electrodes.** *Adv Mater* 2011, **23:**1015–1019.
4. Kuang P, Park JM, Leung W, Mahadevapuram RC, Nalwa KS, Kim TG, Chaudhary S, Ho KM, Constant K: **A new architecture for transparent electrodes: relieving the trade-off between electrical conductivity and optical transmittance.** *Adv Mater* 2011, **23:**2469.
5. Chiappe D, Toma A, de Mongeot FB: **Transparent plasmonic nanowire electrodes via self-organised ion beam nanopatterning.** *Small* 2013, **9:**913–919.
6. Kumar A, Zhou CW: **The race to replace tin-doped indium oxide: which material will win?** *ACS Nano* 2010, **4:**11–14.
7. Wu ZC, Chen ZH, Du X, Logan JM, Sippel J, Nikolou M, Kamaras K, Reynolds JR, Tanner DB, Hebard AF, Rinzler AG: **Transparent, conductive carbon nanotube films.** *Science* 2004, **305:**1273–1276.
8. Feng C, Liu K, Wu JS, Liu L, Cheng JS, Zhang YY, Sun YH, Li QQ, Fan SS, Jiang KL: **Transparent conducting films made from superaligned carbon nanotubes.** *Adv Funct Mater* 2010, **20:**885–891.
9. Wu JB, Becerril HA, Bao ZN, Liu ZF, Chen YS, Peumans P: **Organic solar cells with solution-processed graphene transparent electrodes.** *Appl Phys Lett* 2008, **92:**263302.
10. Eda G, Fanchini G, Chhowalla M: **Large-area ultrathin films of reduced graphene oxide as a transparent and flexible electronic material.** *Nat Nanotechnol* 2008, **3:**270–274.
11. He HY, Li XL, Wang J, Qiu TF, Fang Y, Song Q, Luo B, Zhang XF, Zhi LJ: **Reduced graphene oxide nanoribbon networks: a novel approach**

towards scalable fabrication of transparent conductive films. *Small* 2013, **9**:820–824.
12. Lee JY, Connor ST, Cui Y, Peumans P: **Solution-processed metal nanowire mesh transparent electrodes.** *Nano Lett* 2008, **8**:689–692.
13. Tokuno T, Nogi M, Karakawa M, Jiu JT, Nge TT, Aso Y, Suganuma K: **Fabrication of silver nanowire transparent electrodes at room temperature.** *Nano Res* 2011, **4**:1215–1222.
14. Madaria AR, Kumar A, Zhou CW: **Large scale, highly conductive and patterned transparent films of silver nanowires on arbitrary substrates and their application in touch screens.** *Nanotechnol* 2011, **22**:245201.
15. Rathmell AR, Nguyen M, Chi MF, Wiley BJ: **Synthesis of oxidation-resistant cupronickel nanowires for transparent conducting nanowire networks.** *Nano Lett* 2012, **12**:3193–3199.
16. Kang MG, Park HJ, Ahn SH, Guo LJ: **Transparent Cu nanowire mesh electrode on flexible substrates fabricated by transfer printing and its application in organic solar cells.** *Sol Energ Mat Sol C* 2010, **94**:1179–1184.
17. Kang MG, Park HJ, Ahn SH, Xu T, Guo LJ: **Toward low-cost, high-efficiency, and scalable organic solar cells with transparent metal electrode and improved domain morphology.** *IEEE J Sel Top Quantum Electron* 2010, **16**:1807–1820.
18. Hu L, Wu H, Cui Y: **Metal nanogrids, nanowires, and nanofibers for transparent electrodes.** *MRS Bull* 2011, **36**:760–765.
19. Groep JV, Spinelli P, Polman A: **Transparent conducting silver nanowire networks.** *Nano Lett* 2012, **12**:3138–3144.
20. Lee J, Lee P, Lee H, Lee D, Lee SS, Ko SH: **Very long Ag nanowire synthesis and its application in a highly transparent, conductive and flexible metal electrode touch panel.** *Nanoscale* 2012, **4**:6408–6414.
21. Wu H, Kong DS, Ruan ZC, Hsu PC, Wang S, Yu ZF, Carney TJ, Hu LB, Fan SH, Cui Y: **A transparent electrode based on a metal nanotrough network.** *Nat Nanotechnol* 2013, **8**:421–425.
22. Kwon N, Kim K, Sung S, Yi I, Chung I: **Highly conductive and transparent Ag honeycomb mesh fabricated using a monolayer of polystyrene spheres.** *Nanotechnol* 2013, **24**:235205.
23. Gaynor W, Burkhard GF, McGehee MD, Peumans P: **Smooth nanowire/polymer composite transparent electrodes.** *Adv Mater* 2011, **23**:2905–2910.
24. Tokuno T, Nogi M, Jiu J, Suganuma K: **Hybrid transparent electrodes of silver nanowires and carbon nanotubes: a low-temperature solution process.** *Nanoscale Res Lett* 2012, **7**:281.
25. Koga H, Saito T, Kitaoka T, Nogi M, Suganuma K, Isogai A: **Transparent, conductive, and printable composites consisting of TEMPO-oxidized nanocellulose and carbon nanotube.** *Biomacromolecules* 2013, **14**:1160–1165.
26. Khaligh HH, Goldthorpe IA: **Failure of silver nanowire transparent electrodes under current flow.** *Nanoscale Res Lett* 2013, **8**:235.
27. Li Y, Tsuchiya K, Tohmyoh H, Saka M: **Numerical analysis of the electrical failure of a metallic nanowire mesh due to Joule heating.** *Nanoscale Res Lett* 2013, **8**:370.
28. Xu J, Munari A, Dalton E, Mathewson A, Razeeb KM: **Silver nanowire array-polymer composite as thermal interface material.** *J Appl Phys* 2009, **106**:124310.
29. Liu XH, Zhu J, Jin CH, Peng LM, Tang DM, Cheng HM: **In situ electrical measurements of polytypic silver nanowires.** *Nanotechnol* 2008, **19**:085711.
30. Mayoral A, Allard LF, Ferrer D, Esparza R, Jose-Yacaman M: **On the behavior of Ag nanowires under high temperature: in situ characterization by aberration-corrected.** *STEM J Mater Chem* 2011, **21**:893–898.
31. Alavi S, Thompson D: **Molecular dynamics simulations of the melting of aluminum nanoparticles.** *J Phys Chem* 2006, **110**:1518–1523.
32. Stojanovic N, Berg JM, Maithripala DHS, Holtz M: **Direct measurement of thermal conductivity of aluminum nanowires.** *Appl Phys Lett* 2009, **95**:091905.

doi:10.1186/1556-276X-9-239
Cite this article as: Tsuchiya *et al.*: Consistent melting behavior induced by Joule heating between Ag microwire and nanowire meshes. *Nanoscale Research Letters* 2014 **9**:239.